# Nanometric resolution using far-field optical tomographic microscopy in the multiple scattering regime

Jules Girard,[1] Guillaume Maire,[1] Hugues Giovannini,[1] Anne Talneau,[2] Kamal Belkebir,[1]
Patrick C. Chaumet,[1] and Anne Sentenac[1]

[1]*Institut Fresnel (CNRS UMR 6133), Aix-Marseille Université, F-13013 Marseille, France*
[2]*CNRS, Lab Photon & Nanostruct, F-91460 Marcoussis, France*

The resolution of optical far-field microscopes is classically diffraction-limited to half the illumination wavelength. We show experimentally that this fundamental limit does not apply in the multiple scattering regime. We used tomographic diffractive microscopy at 633 nm to image two pairs of closely spaced rods (with a width and interdistance of 50 nm) of widely different diffractive properties. Using an inversion algorithm accounting for multiple scattering, only the pair of highly diffracting rods could be clearly visualized with a resolution similar to that of an atomic force microscope.

PACS number(s): 42.30.Wb, 42.25.Fx

It is generally accepted that the resolution of far-field optical imagers cannot fall below half the wavelength in the observation medium, $\lambda/2$. This fundamental limit stems from the fact that, for frequencies above $k_0 = 2\pi/\lambda$, the Fourier components of the diffracted field vanish exponentially as they leave the object. Since these evanescent waves encode the high spatial frequency components of the object, their detection is the major challenge of optical imaging. The common strategy of the various techniques that have permitted imaging of nonfluorescent objects with a resolution well beyond the diffraction limit consists in placing the object in the close vicinity of a material probe. This probe can be a subwavelength tip that is moved a few nanometers above the object, as in near-field microscopy [1]. It can also be a structured substrate, viewed as an extended probe, as in grating-assisted microscopy [2,3] or in hyperlens microscopy [4]. In all these cases, the super-resolution is explained by the phenomenon of multiple scattering between the object and the probe. Basically, the evanescent field radiated by the object is scattered by the probe into propagative waves that are detectable in the far field. Conversely, the incident propagative waves can be converted by the probe into high-frequency evanescent fields [2,5–7]. Multiple scattering can also take place within an object made of highly diffracting material. Potentially, such an object could act as a near-field probe for itself. In this case, the question remains whether super-resolved images could be obtained from its sole diffracted far field. This fundamental issue has received particular attention in the past five years [8–10] with mixed or even controversial results due to its complexity. Generally, multiple scattering is seen as a major drawback for imaging as it breaks the linear link between the diffracted field and the object. In this regime, meaningful images cannot be obtained analogically and henceforth advanced inversion procedures are required. The resolution of such numerically reconstructed images is difficult to quantify as it depends on, among other factors, *a priori* information on the object and the noise level [11–13]. Hence, there is still no clear demonstration that multiple scattering can benefit the imaging process in the optical domain.

In this work we show that, in the multiple scattering regime, sub-$\lambda/2$ features of the sample can strongly modify the diffracted far field. Tomographic diffractive microscopy can take advantage of this phenomenon to obtain super-resolved images. As a result, samples made of highly diffracting material could be resolved well beyond the standard $\lambda/2$ limit.

We consider a reflection microscope in which the sample is placed on a glass substrate and possibly illuminated under total internal reflection (Fig. 1). For the sake of simplicity and for illustrative purposes, we assume that the sample is invariant along the $y$ axis and is described by its permittivity contrast $\xi(x,z) = \varepsilon(x,z) - 1$, which can be written as $\eta(x)h(z)$, where $h(z) = 1$ for $0 < z < H$ and 0 elsewhere. The sample is illuminated by a $s$-polarized monochromatic plane wave (in which the electric field is directed along the $y$ axis) in the $(x,z)$ plane depicted by its $x$-component wave vector $\alpha_i = k_0 \sin\theta_i$, where $k_0 = 2\pi/\lambda$ and $\theta_i$ is the incidence angle. From Maxwell's equations, the total electric field $E$ satisfies the self-consistent integral equation [14,15]

$$E(x,z) - E_{\text{ref}}(x,z)$$
$$- \int G(x - x',z,z')\xi(x',z')E(x',z')\,dx'dz' = 0, \quad (1)$$

where $E_{\text{ref}}$ is the field that would exist without the sample and $G(x - x',z,z')$ denotes the field at $(x,z)$ radiated by a line source located at $(x',z')$ above the substrate. Both the diffracted far field and the total field inside the sample can be calculated from Eq. (1). If the sample is weakly diffracting, one can assume that $E \approx E_{\text{ref}}$. This assumption is known as the Born or the single scattering approximation. In this case, straightforward calculations from Eq. (1) show [14] that, if $\lambda \gg H$, the far field diffracted by the sample in the direction specified by the $x$-component wave vector $\alpha_d = k_0 \sin\theta_d$ reads

$$e(\alpha_i,\alpha_d) \propto \tilde{\eta}(\alpha_d - \alpha_i), \quad (2)$$

where $\tilde{\eta}(\alpha)$ is the Fourier transform of $\eta(x)$. The linear relationship between the object and the diffracted field given by Eq. (2) is at the basis of most far-field imaging techniques. Since $|\alpha_i| < k_0$ and $|\alpha_d| < k_0$, spatial frequencies $\alpha$ of the
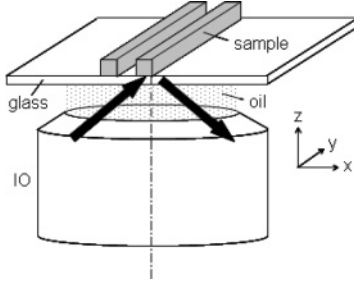
FIG. 1. Reflection microscope: Samples are deposited on a glass substrate and illuminated through the substrate by an immersion objective (IO). The backscattered field is collected by the same IO.

object that are accessible under single-scattering analysis are contained in the interval $\Omega = [-2k_0 \, 2k_0]$. The frequency limit $2k_0$, which is obtained for an imaging configuration allowing grazing illumination and detection, corresponds to the diffraction frequency limit (Abbe's limit).

If the sample is strongly diffracting and multiple scattering is present, the link between the diffracted field and the sample is no longer linear. For example, assuming a double-scattering process, the second-order development of the Born series of Eq. (1) reads [14]

$$e(\alpha_i, \alpha_d) \propto \tilde{\eta}(\alpha_d - \alpha_i)$$
$$+ \int B(\alpha_d, \alpha_i, \alpha) \tilde{\eta}(\alpha - \alpha_i) \tilde{\eta}(\alpha_d - \alpha) \, d\alpha. \quad (3)$$

In this case one observes that the diffracted far field depends on all the spatial Fourier components of the object permittivity contrast. Hence, information on spatial frequencies of the object beyond $2k_0$ could possibly be obtained in the far field if the permittivity contrast is strong enough for the integral term in Eq. (3) to be significant.

To illustrate this assertion, we have considered samples defined by $\eta(x) = \Delta\varepsilon(1 + u\cos Kx)l(x)$, where $l(x) = 1$ for $-L/2 < x < L/2$ and 0 elsewhere. When $u$ is equal to zero, the object is a homogeneous rod of width $L$, height $H$, and permittivity contrast $\Delta\varepsilon$. When $u = -1$ the permittivity contrast of this rod is modulated by a cosine with spatial frequency $K$. From rigorous simulations performed by solving Eq. (1) [15] we represent in Fig. 2 the angular behavior of the intensity of the far field diffracted from homogeneous and modulated rods. Calculations have been performed for an illumination wavelength of 633 nm, $L = 600$ nm, $H = 70$ nm, $K = 5k_0$, $\theta_i = 50°$, and different permittivity contrasts $\Delta\varepsilon = $ 2, 7, and 14. Note that the modulation frequency is larger than twice the Abbe frequency limit. When the contrast is small, the single-scattering approximation is valid and the far field is accurately described by $\tilde{\eta}$. In this case, the intensities of the homogeneous and modulated rods are identical. When $\Delta\varepsilon$ increases, the difference between the homogeneous and modulated rod intensities is strongly accentuated, showing that high-frequency object modulations modify significantly the diffracted far field. Imaging techniques accounting for multiple scattering could thus take advantage of this far-field signature for obtaining super-resolved images.

We have implemented a tomographic diffractive microscopy experiment in which the sample lies on a glass
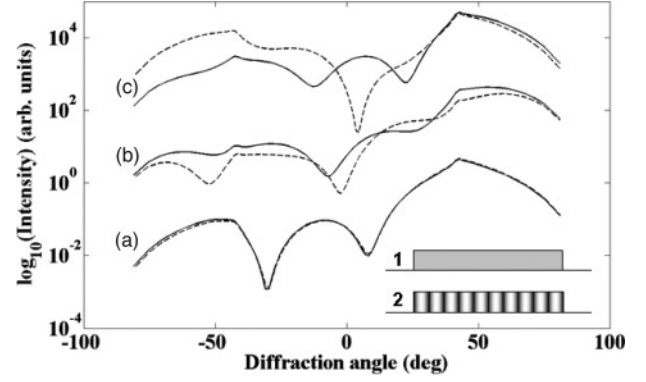


FIG. 2. Computation of the far-field intensity diffracted by a rectangular rod of width 600 nm and height 70 nm, when its permittivity contrast is constant (solid line, inset 1) or modulated by a cosine of spatial frequency $K = 5k_0$ (dashed line, inset 2). The insets represent the sample with $\eta$ in gray scale. The illumination wavelength is 633 nm and the incident angle is 50°. Permittivity contrast values are (a) $\Delta\varepsilon = 2$, (b) $\Delta\varepsilon = 7$, and (c) $\Delta\varepsilon = 14$.

cover and is illuminated through an oil immersion microscope objective (Nikon $\times 40$, numerical aperture NA $= 1.3$) with a collimated laser beam of wavelength 633 nm (see Fig. 1). The backscattered field is collected by the same objective and measured in the rear focal plane using a phase-shifting interferometry technique [11,16]. Far-field measurements are carried out for 10 incidence angles $\theta_i$ and for about 700 observation angles $\theta_d$ distributed over the objective NA.

To retrieve the permittivity map of the sample from the diffracted field, we use an iterative inversion scheme accounting for multiple scattering, described in Refs. [16,17]. At each iteration step, both $\xi$ and $E$ are simultaneously estimated within a box corresponding to the field of view $W$ of the microscope by minimizing a cost function $\mathcal{F}(\xi, E)$ of the form [17]

$$\mathcal{F}(\xi, E) = \frac{\sum_{\theta_i, \theta_d} |\rho_{\text{far}}(\theta_i, \theta_d)|^2}{\sum_{\theta_i, \theta_d} |E_{\text{meas}}(\theta_i, \theta_d)|^2} + \frac{\sum_{\theta_i} \sum_{x, z \in W} |\rho_{\text{near}}(\theta_i, x, z)|^2}{\sum_{\theta_i} \sum_{x, z \in W} |E_{\text{ref}}(\theta_i, x, z)|^2}. \quad (4)$$

$E_{\text{meas}}$ is the measured scattered far field, $\rho_{\text{far}}$ is the difference between $E_{\text{meas}}$ and the simulated far field for the estimates of $\xi$ and $E$, and $\rho_{\text{near}}$ is the left-hand side of Eq. (1) evaluated with the same estimates of $\xi$ and $E$. The minimization of $\rho_{\text{near}}$ ensures that the field inside the sample is accurately computed even when multiple scattering is present.

Like all inversion procedures, our reconstruction algorithm assumes the finite extent of the object (indicated by the investigating domain $W$). Now, it is known that, if the sample is bounded, images with infinite resolution can theoretically be obtained from the diffracted far field even under the single-scattering approximation because of the analycity of $\tilde{\eta}$ [18]. However, the inversion process, which consists in extending $\tilde{\eta}$ in the whole Fourier space from its known restriction in $\Omega$, is curtailed by the presence of noise [13]. Therefore, in practice, it does not permit a significant improvement of the resolution beyond the Abbe limit. Adding more *a priori* information on the object is another way to improve the quality and the resolution of the reconstructions [12]. Here, only the positivity

of the object permittivity contrast is used in the algorithm. Yet, this comment highlights the difficulty in assessing the origin of the resolution improvement when numerical reconstruction procedures are used inasmuch as the noise, the size of $W$, and the amount of *a priori* knowledge all play a crucial role.

To overcome this issue, we have considered two samples with the same topography but with different permittivities so that one falls within the single-scattering approximation whereas the other supports significant multiple scattering (Fig. 3). The samples consist of two rods of a width of 50 nm, a height of 25 nm, and a separation distance of 50 nm. These dimensions fall far below the Abbe limit of the imager. The relative permittivity of the highly scattering sample is $29.8 + i7.3$, which corresponds to germanium at 633 nm, and that of the low contrast object is 1.01. We have checked that the permittivity losses play a negligible role with such object dimensions. We first plot in Figs. 3(a) and 3(b) the modulus of the field $|E|$ within $W$ obtained by solving Eq. (1) for both samples with a total internal reflection illumination at $\theta_i = -50°$. As expected, $|E|$ is close to the reference field modulus $|E_{ref}|$ for the weakly contrasted sample and very different from $|E_{ref}|$ for the highly diffracting rods. In this latter case, one observes a hot subdiffraction spot localized in one rod. Varying $\theta_i$ induces a displacement of the spot within the object. Unsurprisingly, the far field (not shown) diffracted by the weakly scattering rods is very different from that diffracted by the strongly scattering rods in shape, modulus (with one being 2000 times higher than the other), and phase.

We display in Fig. 3(c) the reconstructed permittivity obtained by the nonlinear inversion algorithm for the weakly diffracting rods. The far-field data used in the inversion procedure were simulated with Eq. (1) so that they were only spoiled by numerical errors (discretization and truncature). We stopped the inversion procedure when the minimized cost function $\mathcal{F}$ reached a value about 1%. We observe that, even without noise and with the *a priori* knowledge of finite extent of the object and positivity of its permittivity contrast, the reconstruction scheme fails in separating the two rods. We then studied the case of the highly diffracting rods using the same data simulation and inversion procedures. In this case, the two highly diffracting rods could be clearly resolved (results not shown). To confirm this result experimentally, measurements were performed with the tomographic diffractive microscope on germanium rods. The rods were fabricated by electron beam lithography, coupled to reactive ion etching and lift-off techniques, and characterized after the fabrication with a scanning electron microscope. The experimental noise, evaluated as the squared modulus of the relative difference between the simulated and the measured diffracted fields, reaches 39%. During the inversion, $\mathcal{F}$ did not decrease below 28%. Yet, the two rods could be easily separated on the reconstructed map of permittivity [Fig. 3(d)]. For comparison, we have plotted in Fig. 3(d) the atomic force microscope (AFM) profile of the sample, which confirmed that both the transverse and axial dimensions of the rods were accurately retrieved. Figures 3(e) and 3(f) show the permittivity profile along the white dashed line of Figs. 3(c) and 3(d), respectively, and Fig. 3(g) presents the normalized modulus of the Fourier transforms of these permittivity profiles, as a function of the transverse spatial frequency in $k_0$ units. While the object
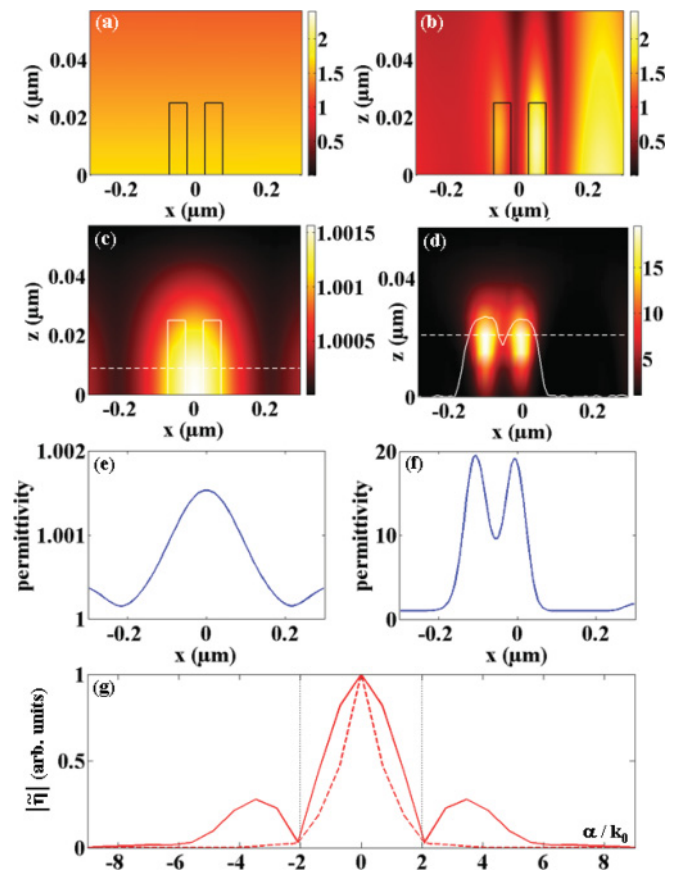


FIG. 3. (Color online) Imaging of two rods (width = 50 nm, height = 25 nm, and interdistance = 50 nm) in the single or multiple scattering regimes. (a, c, e) The rods have a relative permittivity of 1.01. (b, d, f) The rods have a relative permittivity of $29.8 + i7.3$ (germanium at 633 nm). (a, b) Map of the electric field modulus $|E|$ simulated inside the investigation domain $W$ for an incident angle of $-50°$. (c) Permittivity map reconstructed from simulated far-field data (where the solid white line is the actual height profile). (d) Permittivity map reconstructed from the experimental data obtained with the tomographic diffractive microscope (where the solid white line is the experimental AFM height profile of the same sample). (e, f) Permittivity profile along the dashed white line shown in (c) or (d). (g) Normalized modulus of the Fourier transform of the permittivity profile of (e) (dashed line) and (f) (solid line); spatial frequencies are shown in $k_0$ units; dotted vertical lines indicate the Abbe frequency limit.

spatial frequencies are not retrieved beyond the Abbe limit (dotted vertical lines) in the low-permittivity case (dashed line), they are accurately estimated in an extended range up to three times the Abbe limit in the high-permittivity case (solid line). We believe that this achievement is due to the multiple scattering phenomenon, which yields a selective illumination of the rods depending on the incident angle, as seen in Fig. 3(b). Actually, this subdiffraction light spot that first focuses on one rod and then moves to the other is quite similar to that which would be generated by a scanning near-field probe [1]. This observation points out the major issue of imaging techniques in the multiple scattering regime: Their performances depend on how the internal field probes the sample when the incidence angle is varied. In Fig. 4(a) we
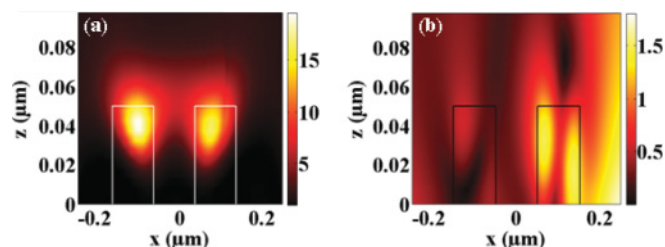
FIG. 4. (Color online) (a) Reconstructed permittivity map for two rods spaced by 100 nm, with a width of 100 nm and a height of 50 nm. (b) Modulus of the field $|E|$ simulated when the rods are illuminated at $-50°$.

plot the reconstructed permittivity obtained from experimental data of two germanium rods spaced by 100 nm, with width of 100 nm and a height of 50 nm (where the white line represents the actual height profile). The simulated total field modulus $|E|$ in $W$ displayed in Fig. 4(b) shows that, similarly to Fig. 3(b), multiple scattering yields subdiffraction bright spots that are likely to probe the fine details of the object. Yet, the total field intensity averaged in $W$ over all the incidence angles is mostly localized at the top of the rods (result not shown).

As a result, the reconstructed permittivity is localized in this region. However, it still provides accurate estimates of the height, width, and interdistance of the rods.

Hence, with these highly diffracting samples, our approach was able to distinguish rods heights of 25 and 50 nm, rod widths of 50 and 100 nm, or rod interdistances of 50 and 100 nm. This achievement demonstrates that the power of resolution of digital far-field microscopes in the multiple scattering regime can be much better than the classical Abbe limit provided inversion algorithms based on a rigorous modeling of the wave-sample interaction are used. The quality of the retrieved permittivity maps could be further improved by using additional *a priori* knowledge of the sample [12] and regularization terms in Eq. (4) [19]. The main issue is that the resolution limit of this approach cannot be easily defined as it depends both on the optical setup and on the sample under study. Yet, we believe that this method could be most interesting for imaging nanostructured devices like those manufactured in the microelectronic domain.

[1] F. de Fornel, *Evanescent Waves: From Newtonian Optics to Atomic Optics*, vol. 73 of Optical Sciences Series (Springer-Verlag, Berlin, 2001).

[2] A. Sentenac, P. C. Chaumet, and K. Belkebir, Phys. Rev. Lett. **97**, 243901 (2006).

[3] Z. Liu, S. Durant, H. Lee, Y. Pikus, N. Fang, Y. Xiong, C. Sun, and X. Zhang, Nano Lett. **7**, 403 (2007).

[4] Z. Liu, H. Lee, L. Xiong, C. Sun, and X. Zhang, Science **315**, 1686 (2007).

[5] G. Lerosey, J. de Rosny, and M. Fink, Science **315**, 1120 (2007).

[6] A. Sentenac and P. C. Chaumet, Phys. Rev. Lett. **101**, 013901 (2008).

[7] M. J. Steel, B. Marks, and A. Rahmani, Opt. Express **18**, 1487 (2010).

[8] A. Sentenac, C.-A. Guérin, P. C. Chaumet, F. Drsek, H. Giovannini, N. Bertaux, and M. Holschneider, Opt. Express **15**, 1340 (2007).

[9] F. Simonetti, Phys. Rev. E **73**, 036619 (2006).

[10] J. de Rosny and C. Prada, Phys. Rev. E **75**, 048601 (2007).

[11] G. Maire, F. Drsek, J. Girard, H. Giovannini, A. Talneau, D. Konan, K. Belkebir, P. C. Chaumet, and A. Sentenac, Phys. Rev. Lett. **102**, 213905 (2009).

[12] P. C. Chaumet, K. Belkebir, and A. Sentenac, J. Appl. Phys. **106**, 034901 (2009).

[13] P. J. Sementilli, B. R. Hunt, and M. S. Nadar, J. Opt. Soc. Am. A **10**, 2265 (1993).

[14] C.-A. Guérin and A. Sentenac, J. Opt. Soc. Am. A **21**, 1251 (2004).

[15] J.-J. Greffet, Opt. Commun. **72**, 274 (1989).

[16] G. Maire, J. Girard, F. Drsek, H. Giovannini, A. Talneau, K. Belkebir, P. C. Chaumet, and A. Sentenac, J. Mod. Opt. **57**, 746 (2010).

[17] K. Belkebir and A. Sentenac, J. Opt. Soc. Am. A **20**, 1223 (2003).

[18] G. Toraldo di Francia, J. Opt. Soc. Am. **45**, 497 (1955).

[19] K. Belkebir and M. Saillard, Inverse Probl. **21**, S1 (2005), and references therein.